

Evolution of magnetic deformation in neutron star crust

Yasufumi Kojima¹, * Shota Kisaka^{1,2,3}, Kotaro Fujisawa⁴

¹*Department of Physics, Hiroshima University, Higashi-Hiroshima, Hiroshima 739-8526, Japan*

²*Frontier Research Institute for Interdisciplinary Sciences, Tohoku University, Sendai, 980-8578, Japan*

³*Astronomical Institute, Graduate School of Science, Tohoku University, Sendai, 980-8578, Japan*

⁴*Research Center for the Early Universe, Graduate School of Science, University of Tokyo, Bunkyo-ku, Tokyo 113-0033, Japan*

9 November 2020

ABSTRACT

In this study, we examine the magnetic field evolution occurring in a neutron star crust. Beyond the elastic limit, the lattice ions are assumed to act as a plastic flow. The Ohmic dissipation, Hall drift, and bulk fluid velocity driven by the Lorentz force are considered in our numerical simulation. A magnetically induced quadrupole deformation is observed in the crust during the evolution. Generally, the ellipticity decreases as the magnetic energy decreases. In a toroidal-field-dominated model, the sign of the ellipticity changes. Namely, the initial prolate shape tends to become oblate. This occurs because the toroidal component decays rapidly on a smaller timescale than the poloidal dipole component. We find that the magnetic dipole component does not change significantly on the Hall timescale of ~ 1 Myr for the considered simple initial models. Thus, a more complex initial model is required to study the fast decay of surface dipoles on the abovementioned timescale.

Key words: stars: neutron – stars: magnetic fields – stars: magnetars

1 INTRODUCTION

The magnetic field strength of a single neutron star ranges from 10^8 to 10^{15} G (Turolla et al. 2015; Enoto et al. 2019). Neutron stars exhibit different phenomena, based on which they are broadly classified. The diversity of the classes could be simply attributed to their formation and environment. It is also known that the activity of magnetars, a class of strongly magnetized stars, originates from their magnetic energy. Therefore, the magnetic field is not constant in some neutron stars of ages $\sim 10^4$ – 10^5 yr. In a theoretical study, it is important to understand the extent of the magnetic field change on the abovementioned timescale.

The physics of the magnetic field evolution in neutron stars is discussed in a classical paper (Goldreich & Reisenegger 1992). The evolution is determined by the advection and dissipation of the magnetic field. Typically, numerical simulations are required because of the nonlinear nature of the coupled equations. In a neutron star core, the Ohmic dissipation is less effective owing to the high conductivity. For a fast evolution on the timescale of $< 10^6$ yr, the transportation of the magnetic flux to the lower conductivity region in the crust or near the surface is important. The core of a neutron star comprises multi-components; it is primarily a fluid mixture of neutrons, protons, and electrons, whose number densities vary from the center to the crust. In a weak-coupling regime, they can move with different velocities so that the transport velocity is multiple. In addition, the effects of the superfluidity and superconductivity in the core increase the complexity of the relevant physics. Although this challenging issue has been addressed in the past (e.g., Glampedakis et al. 2011; Graber et al. 2015; Elfriz et al. 2016; Gugercinolu & Alpar 2016; Passamonti et al. 2017; Castillo et al. 2017; Bransgrove et al. 2018), it is still being debated (Gusakov et al. 2017; Kantor & Gusakov 2017; Ofengeim & Gusakov 2018; Gusakov 2019; Castillo et al. 2020).

The physics of the crustal magnetic field is comparatively simple. In the solid crust, the lattice ions are fixed, and only the electrons are mobile. The magnetic field evolution due to the Hall drift and the Ohmic dissipation has been investigated by several researchers. A magnetic field with an axial symmetry was numerically simulated on a secular timescale (e.g., Pons & Geppert 2007; Kojima & Kisaka 2012; Viganò et al. 2013). Evolution to an equilibrium configuration and its stability were discussed in (Gourgouliatos et al. 2013; Gourgouliatos & Cumming 2014a,b; Marchant et al. 2014). Recently, the numerical simulation of the long-term magnetic-field evolution has been extended to three-dimensional models (Wood & Hollerbach 2015; Gourgouliatos et al. 2016; Gourgouliatos & Hollerbach 2018; Viganò et al. 2019), revealing some of the effects ignored in the two-dimensional models.

* E-mail: ykojima-phys@hiroshima-u.ac.jp

In this study, we explore the effects of the plastic flow in the crust of a neutron star. In some strongly magnetized stars, the field strength is extremely high, deforming the lattice structure of the ions by the shear stress. A crust responds elastically when its deformation is within a critical limit, beyond which it cracks or responds plastically. The breaking strain determined by molecular dynamics simulations (Horowitz & Kadau 2009) is ~ 0.1 , whereas semi-analytical methods (Chugunov & Horowitz 2010; Baiko & Chugunov 2018) give a smaller value < 0.04 . Abrupt crust breaking can cause a magnetar outburst and/or a rapid radio burst (Lander et al. 2015; Li et al. 2016; Suvorov & Kokkotas 2019, 2020; Ioka 2020). Thus, understanding the response of the crust of a neutron star is crucial for improving its astrophysical modelling.

The plastic flow beyond the critical limit was explicitly demonstrated by a long-term simulation of a two-dimensional box (Lander & Gourgouliatos 2019), and the effect of the large-scale velocity circulation occurring in an axially symmetric crust was explored (Kojima & Suzuki 2020, hereafter referred as Paper I). The resultant bulk velocity was approximately proportional to the square of the magnetic field strength, whereas the Hall velocity varied linearly with the strength. Therefore, in magnetars or neutron stars with a hidden strong field, the effect of the plastic flow on the crustal field evolution is important. We assume that the plastic flow occurs at all times in the entire crust. Actual neutron star crust might be a mixture of the elastic/plastic responding regions, since magnetic stress depends on the place, and exceeds a threshold somewhere. The flow velocity v_b therefore arises not in the entire crust but in super-critical region only. For such a partially flowing structure, we have to solve an elliptic equation explained in next section with the constrain $v_b = 0$ in the elastic region. The numerical method becomes more complicated, and the solution may contain local irregularities. Our concern is a global aspect so that we compare a flowing model ($v_b \neq 0$) in the entire crust with no flowing model, i.e. the Hall evolution model. Realistic model probably corresponds to the intermediate between these limiting cases.

In this study, we also investigate the effect of the strong magnetic field in a neutron star crust. It is well known that strong magnetic fields deform stellar shapes. We numerically simulate the time evolution of a quadrupole deformation. This problem was previously studied by Suvorov et al. (2016), who claimed that large deformations can occur in normal radio pulsars having a surface dipole field of 10^{12} – 10^{13} G. Some neutron stars experience a large quadrupole deformation owing to a hidden field, which is unrelated to the inferred dipole strength. This topic is extremely important in gravitational wave astronomy (e.g. Gao et al. 2017; Kalita & Mukhopadhyay 2019). Namely, potential sources for continuous gravitational waves in near future detection are revealed. Our approach to calculate the magnetic deformation is different from that in the referred study; therefore, it is important to compare the results from both the methods. The models and the equations of this study are presented in Section 2. In Section 3, the numerical results of the magnetic energy and the surface dipole moment are discussed. In Section 4, the quadrupole deformation of a neutron star crust is described. Finally, our concluding remarks are presented in Section 5.

2 MATHEMATICAL FORMULATION

When a magnetized neutron star is born, all the forces are in equilibrium on a short dynamical timescale. The magneto-hydrodynamic (MHD) equilibrium among the pressure, gravity, and Lorentz force is expressed as

$$-\vec{\nabla}P - \rho\vec{\nabla}\Phi_G + \delta\vec{f} = 0, \quad (1)$$

where magnitude of the last term, $\delta\vec{f} \equiv c^{-1}\vec{j} \times \vec{B}$, is $\sim 10^{-7}(B/10^{14}\text{G})^2$ times smaller than those of the first and second terms. We ignore the stellar rotation. Any deviation from the static shape with spherical symmetry is sufficiently small to be considered as a perturbation in the background equilibrium. Equation (1) expressing a spherical equilibrium is reduced to

$$\frac{dP}{dr} = -\frac{G\rho M_r}{r^2}, \quad (2)$$

where M_r is the mass contained within a sphere of radius r . This study is limited to an axially symmetric magnetic field configuration. The poloidal and toroidal components of the magnetic field are expressed as

$$\vec{B} = \vec{\nabla} \times \left(\frac{\Psi}{\varpi} \vec{e}_\phi \right) + \frac{S}{\varpi} \vec{e}_\phi, \quad (3)$$

where $\varpi = r \sin \theta$ is the cylindrical radius. Under barotropic MHD equilibrium, the current function, S , should be a function of Ψ , and the azimuthal current is expressed as (Tomimura & Eriguchi 2005; Gourgouliatos et al. 2013; Fujisawa & Kisaka 2014)

$$\frac{4\pi\varpi}{c} j_\phi = -\rho K' \varpi^2 - S' S. \quad (4)$$

In Eq.(4), K is also a function of Ψ , and a prime denotes a derivative with respect to Ψ . The Lorentz force is defined as

$$\delta\vec{f} = \rho K' \vec{\nabla} \Psi. \quad (5)$$

For given functional forms $S(\Psi)$ and $K(\Psi)$, the magnetic function, Ψ , which describes the poloidal field, \vec{B}_p , by eq.(3), is solved for the source term (4). Although this method is simple, the actual calculations are difficult. It is not possible to obtain the solution for arbitrary forms of $S(\Psi)$ and $K(\Psi)$. Presumably, the barotropic condition highly constrains static models.

In an MHD equilibrium, electrons are not in equilibrium; therefore, the magnetic field tends to a configuration determined by

the Hall equilibrium on a secular timescale (Gourgouliatos et al. 2013; Gourgouliatos & Cumming 2014b). The Lorentz force, $\vec{j} \times \vec{B}$, is not fixed but changes according to the magnetic field evolution, which is governed by the induction equation,

$$\frac{\partial}{\partial t} \vec{B} = -\vec{\nabla} \times (c\vec{E}), \quad (6)$$

where

$$c\vec{E} = \frac{c}{\sigma} \vec{j} + \frac{1}{en_e} \vec{j} \times \vec{B} - \vec{v}_b \times \vec{B}. \quad (7)$$

In eq.(7), σ is the electric conductivity, n_e the electron number density, and \vec{v}_b the bulk flow velocity. The latter may be approximated as the ion velocity owing to the large mass difference between ions and electrons. In a comoving frame of a neutron star, the ions in the crust are fixed in the lattice, i.e., $\vec{v}_b = 0$. In this case, the dynamics expressed in eq.(6) is determined by the magnetic field because of its relation to the electric current, \vec{j} , by Ampère–Bio-Savart’s law as follows:

$$\vec{j} = \frac{c}{4\pi} \vec{\nabla} \times \vec{B}. \quad (8)$$

The magnetic field evolution changes the structure and disrupts the abovementioned force equilibrium. This process may be slow or abrupt, depending on the material property. When a magnetic stress exceeds a threshold, the crust may be fractured, and the magnetic field is rearranged. Abrupt crust-quakes can cause a magnetar outburst and/or a rapid radio burst. In this study, we consider the opposite case. Specifically, we treat the gradual deforming motion of the lattice ions as a plastic flow, whose velocity is expressed by \vec{v}_b . The effect of the magnetic field evolution is added as a new velocity component \vec{v}_b in eq.(7). The method to determine \vec{v}_b is described in Paper I (Kojima & Suzuki 2020). Here, we briefly explain the basic concept of the proposed procedure. The Lorentz force, $\delta\vec{f}(\equiv c^{-1}\vec{j} \times \vec{B})$, is generally decomposed as a sum of irrotational and solenoidal vectors as follows:

$$\delta\vec{f} = -\vec{\nabla}\delta\chi + \vec{\nabla} \times (\delta\vec{A}). \quad (9)$$

The scalar potential, $\delta\chi$, and the vector potential, $\delta\vec{A}$, satisfy

$$\nabla^2 \delta\chi = -\vec{\nabla} \cdot \delta\vec{f}, \quad (10)$$

$$\vec{\nabla} \times \vec{\nabla} \times \delta\vec{A} = \vec{\nabla} \times \delta\vec{f}. \quad (11)$$

The potential, $\delta\chi$, is closely coupled to the pressure and gravity terms in eq.(1). However, the solenoidal part of $\delta\vec{f}$ is almost irrelevant for these dominant forces. It drives a shear flow and leads to a nonbarotropic distribution, $\vec{\nabla}(P + \delta P) \times \vec{\nabla}(\rho + \delta\rho) \neq 0$. The force in a strongly magnetized star may deform its crust plastically. This effect is incorporated as an extra viscous flow term in the equation of motion, and the dynamics is expressed by the standard Navier–Stokes equation (Lander 2016; Lander & Gourgouliatos 2019). The solenoidal part of the Lorentz force is assumed to be balanced by the shear stress of the viscous bulk motion (see Paper I) An incompressible fluid approximation is also assumed for simplicity. Because our focus is on the long-term behavior of the magnetic field, all the forces are always approximated to be instantaneously balanced. Therefore, the velocity field structure is determined under a stationary condition. The balance between the viscous fluid motion and the Lorentz force suggests that the bulk velocity field, v_b , depends on $\propto \nu^{-1}B^2$, where ν is the viscous coefficient and B is the typical magnetic field strength. The Hall velocity, $v_H \equiv |j/(en_e)|$, is proportional to B . Eq.(7) contains two advection velocities; however, the bulk velocity, v_b , is important in low-viscosity and strong-magnetic-field regimes. The former condition is generally satisfied near the stellar surface. We found that the typical value of $\nu = 10^{36} - 10^{37} \text{gcm}^{-1}\text{s}^{-1}$ is important for a magnetized neutron star with $B_0 \sim 5 \times 10^{13} \text{G}$ at the pole (Lander & Gourgouliatos 2019, Paper I). Herein, the behavior on the smaller timescale ($\propto v_b^{-1}$) associated with bulk motion is explored.

This study also examines the effect of the time variation of the irrotational part of the Lorentz force. The potential, $\delta\chi$, is important for magnetic deformation because it may be regarded as an additional pressure term in eq.(1). Its effect on the magnetic field evolution is less clear because it strongly depends on the responses of the dominant forces. Herein, we ignore this, and only in Section 4 present the study of the magnetic deformation using evolutionary models free from the irrotational part.

3 EVOLUTION OF MAGNETIC ENERGY

In this section, we consider the effect of the bulk fluid motion on the magnetic evolution. Specifically, the magnetic field evolution of a purely Hall evolution is determined by eqs. (6),(7), and (8) with $\vec{v}_b = 0$. The effect of the bulk motion is incorporated in eq. (7) by including \vec{v}_b , which is determined by the solenoidal part of the Lorentz force. Two types of evolutionary models are compared.

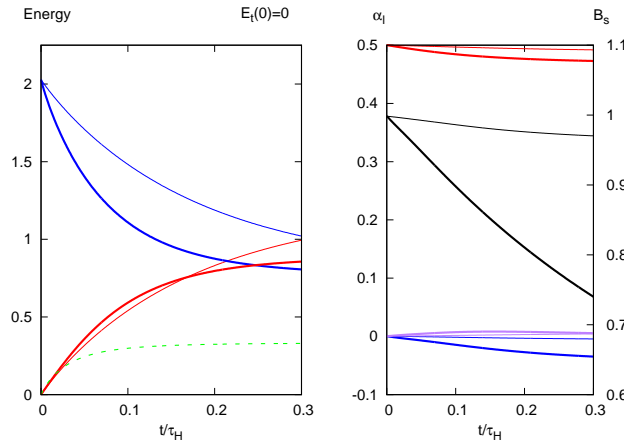


Figure 1. Left panel shows decay of magnetic energy. Magnetic energy $E_B/(B_0^2 R^3)$ is plotted as decreasing curve (in blue color), time-integrated Joule loss as increasing curve (in red color), and work to bulk motion as dotted curve (in green color). Right panel displays time-variation in magnetic multipole moments, $\alpha_1/(B_0 R^3)$ (in red color), $\alpha_3/(B_0 R^5)$ (in blue color), $\alpha_5/(B_0 R^7)$ (in purple color). Field strength B_r/B_0 at polar surface with right scale is plotted by black curve. Thick curves represent model in which bulk motion is considered.

3.1 Barotropic MHD equilibrium

For the initial magnetic field configuration, a reasonable assumption is barotropic MHD equilibrium, for which the azimuthal current is expressed in eq.(4). The solution for a purely poloidal field ($S = 0$) with a constant K' is easily obtained. We denote the solution as $\Psi_{(1)}$ and the current as $j_{\phi(1)} \equiv -c\rho K' \varpi / 4\pi$. For this case, the angular dependence of the magnetic field is dipolar, i.e., $\Psi_{(1)} (\propto \sin^2 \theta)$ is expressed by a single Legendre polynomial of $l = 1$. During the magnetic evolution, a toroidal magnetic field is generally induced, and the symmetry with respect to the angular dependence is not conserved owing to the nonlinear coupling terms in eqs. (6)–(7). We first discuss the magnetic field evolution from the initial state, $\Psi_{(1)}$, in the crust. This model is referred as the fiducial model. The initial magnetic field and current distribution were demonstrated in Fig.1 of Paper I¹.

Below, we briefly discuss the model. Our consideration is limited to a stellar model with the crustal thickness $\Delta r/R = 0.1$, where R is the radius. The size depends on the mass or the equation of state of high density-matter. We also ignore effects of general relativity and temperature. More realistic treatments lead to some modifications. The difference is a few in the magnitude, and overall property is unchanged. Rather, the ambiguity associated with the strength and configuration of magnetic field is larger than that with these approximations. We assume that the magnetic field is always expelled from the core, and for a fixed crustal model, focus on the effects of the initial magnetic field on its evolution. Electron number density n_e , conductivity σ in eq.(7), and viscous coefficient ν in the crust have the same functional forms given in eqs.(28)–(30) in Paper I. For the normalization of time, we use $\tau_H = 6.9 \times 10^5 (B_0/5 \times 10^{13} \text{G})^{-1} \text{yr}$ ², which is the Hall timescale calculated by the field configuration, $\Psi_{(1)}$, using the magnetic field strength, B_0 , at the poles ($r = R, \theta = 0$). The typical Ohmic dissipation time defined by the electronic conductivity at the core–crust interface is $\tau_{\text{Ohm}} = 5.7 \times 10^6 \text{yr}$. However, the actual dissipative time is much shorter than τ_{Ohm} because the conductivity decreases toward the surface. The Ohmic time is also proportional to the square of the spatial size, and hence, the local irregularity is expected to be smoothed on a smaller timescale.

The magnetic field evolution for the initial model, $\Psi_{(1)}$, is shown in Fig. 1. The left panel displays the evolution of the magnetic energy, E_B , which is normalized by $B_0^2 R^3 = 3 \times 10^{45} (B_0/5 \times 10^{13} \text{G})^2 \text{erg}$. The magnetic energy decreases by half at $t \approx 0.3\tau_H = 2 \times 10^5 (B_0/5 \times 10^{13} \text{G})^{-1} \text{yr}$. The thick lines represent the results when the bulk motion in the crust is considered. The magnetic energy is further decreased on being converted to mechanical motion. The behavior of the time-integrated Joule loss is almost unchanged irrespective of the viscous bulk flow. We typically examine energy conservation in our numerical calculation. The magnetic energy loss is the sum of the time-integrated Joule loss and the mechanical work for the bulk motion. A significant amount of energy is converted into mechanical motion. For example, although the total work is $0.4B_0^2 R^3$ at $0.3\tau_H$, this is not necessarily the amount of kinetic energy of the bulk motion at $0.3\tau_H$. In actual cases, the energy is dissipated through

¹ Animation of time-variation of the Lorentz force is available in the online version. Three components during the Hall evolution of the fiducial model are shown by color contour.

² For the discussion, we adopt an intermediate value between a magnetar and a pulsar, $5 \times 10^{13} \text{G}$,

bursts, flares, or other processes, which are not treated here. Regardless of the detailed process, energy is transferred to the bulk motion, and the magnetic energy loss is enhanced.

The exterior of the star is assumed to be vacuum. The external magnetic field is described by a sum of the multipoles,

$$\vec{B} = -\vec{\nabla} \left(\sum \frac{\alpha_l}{r^{l+1}} P_l \right), \quad (12)$$

where $P_l(\cos\theta)$'s are Legendre polynomials, and the multipole moments, α_l , are calculated by matching to the interior component B_r . The time evolution of $\alpha_l/(B_0 R^{l+2})$ ($l = 1, 3, 5$) is shown in the right panel of Fig. 1. The moments with even number l vanish owing to a symmetry. The dipole moment slightly decreases and higher moments grow with time. We also display the magnetic field strength at the poles ($\theta = 0, \pi$), i.e., $B_s = B_r(R, 0)$. Note that for a dipolar field, $B_r(R, 0) = -B_r(R, \pi)$. Although both α_1 and B_s decrease with time, they are not equal. The field strength, B_s , at the polar caps decreases more rapidly than the dipole moment, α_1 . This difference can be attributed to B_s containing the contribution of higher multipole components, which are produced by the nonlinear coupling in the evolutionary equation: $B_s \approx 2\alpha_1 R^{-3} + 4\alpha_3 R^{-5} + 6\alpha_5 R^{-7}$. In the model including the bulk motion, B_s decreases by $\sim 25\%$ at $t \approx 0.3\tau_H$ and α_1 by $\sim 5\%$.

3.2 Model containing poloidal closed field

We consider another initial model that deviates from the barotropic MHD equilibrium. Although the magnetic field is purely poloidal, it has a loop structure, as depicted in Fig. 2. We add the field, $\Psi_{(2)}$, to $\Psi_{(1)}$, in the fiducial model as follows:

$$\Psi_{(2)} = N_1[(r - r_c)(r - R)]^2 \sin^2 \theta, \quad (13)$$

where $r_c (= 0.9R)$ is the core radius and N_1 is the normalization constant. The initial current is accordingly changed as $j_{\phi(1)} + j_{\phi(2)}$, where $j_{\phi(2)}$ is associated with $\Psi_{(2)}$. The total magnetic energy may increase on changing N_1 . However, the magnetic field at the surface is unchanged from that of $\Psi_{(1)}$, because the function (13) and its derivative vanish at the surface.

We demonstrate the effect of the extra field, $\Psi_{(2)}$, for which $N_1 = 3.2 \times 10^4 B_0 R^{-2}$ is used. The maximum field strength is $\sim 22B_0$ due to $\Psi_{(2)}$, and the maximum position is $(r, \theta) \approx ((r_c + R)/2, \pi/2)$. Figure 2 shows the Hall evolution for two initial models: $\Psi_{(1)}$ in the left two panels and $\Psi_{(1)} + \Psi_{(2)}$ in the right two panels. To display a detailed structure, the crustal region, $(r \sin\theta, r \cos\theta)$, ($0.9 \leq r/R \leq 1$) is enlarged five times in the figure as $(\xi(r) \sin\theta, \xi(r) \cos\theta)$, where $\xi = 1 + (R - r)/(2\Delta r)$ and $\Delta r/R = 0.1$. The poloidal magnetic field and the azimuthal current are displayed at their representative times $t/\tau_H = 0.01$ and 0.3. A large amount of the current is initially stored in the model containing the loop. By including $j_{\phi(2)}$, the maximum point of j_{ϕ} is shifted to the middle of the crust, where Ψ is the largest. At time $t = 0.3\tau_H$, the loop structure vanishes, and a large amount of the current is dissipated. The magnetic function becomes approximately the same as that in the fiducial model. The difference between the initial models is not clear at $t = 0.3\tau_H$.

Figure 3 shows the evolution of the magnetic energy. The initial value of $E_B/(B_0^2 R^3) = 4$ decays to $E_B/(B_0^2 R^3) \sim 1$ at $t = 0.3\tau_H$. The energy at $0.3\tau_H$ is almost the same as that considered in Fig. 1. The decay curve becomes steeper than that for the fiducial model; however, most of the energy dissipated during this period is associated with the initial extra components, $\Psi_{(2)}$ and $j_{\phi(2)}$. The long-lived component is unchanged irrespective of the initial models, $\Psi_{(1)}$ or $\Psi_{(1)} + \Psi_{(2)}$, as inferred from Fig. 2. In the right panel of Fig. 3, the evolution of the field strength, B_s , at the polar caps and the dipole moment, α_1 , are shown. The poloidal field initially confined in the interior slightly enhances their decrease.

3.3 Model containing large toroidal field

The initial model considered in the previous subsections considered a purely poloidal magnetic field. Generally, a toroidal component is produced during the magnetic field evolution; however, it is significantly weaker than the poloidal one. The maximum of the toroidal field is one order of magnitude smaller than that of the poloidal field. The angular dependence of magnetic field near the surface is typically approximated by the dipolar field. It is important to study how these behaviors may change with the initial toroidal magnetic field. However, it is difficult to construct toroidal-field-dominated models that satisfy the MHD equilibrium condition. To examine the effect of a large toroidal field confined to a crust, we add the following toroidal component to the fiducial model described in Section 3.1:

$$S = (r \sin\theta) B_{\phi} = N_2[(r - r_c)(r - R)]^2 \sin^2 \theta, \quad (14)$$

where N_2 is the normalization constant. By increasing N_2 , we construct models with a strong toroidal field. However, the state does not satisfy the barotropic MHD equilibrium condition (see eq.(4)). Specifically, the poloidal field, $\Psi_{(1)}$, is not a solution for eq. (4) and $S \neq S(\Psi_{(1)})$.

Figure 4 shows the evolution of the model in which the toroidal magnetic energy is initially dominated. We use $N_2 = 3.1 \times 10^2 B_0 R^{-3}$, and the maximum of B_{ϕ} is $\sim 20B_0$, which is comparable to that of poloidal component. The magnetic energy ratio of the toroidal and poloidal components is initially $E_t/E_p = 2.5$. The time evolutions of E_p and E_t are shown in the left panel of Fig. 4. The energy transfer from the toroidal to poloidal components occurs only in the early times at $\approx 0.01\tau_H$. The toroidal energy decays extremely rapidly; therefore, the increase in the poloidal energy, which is transferred during the early

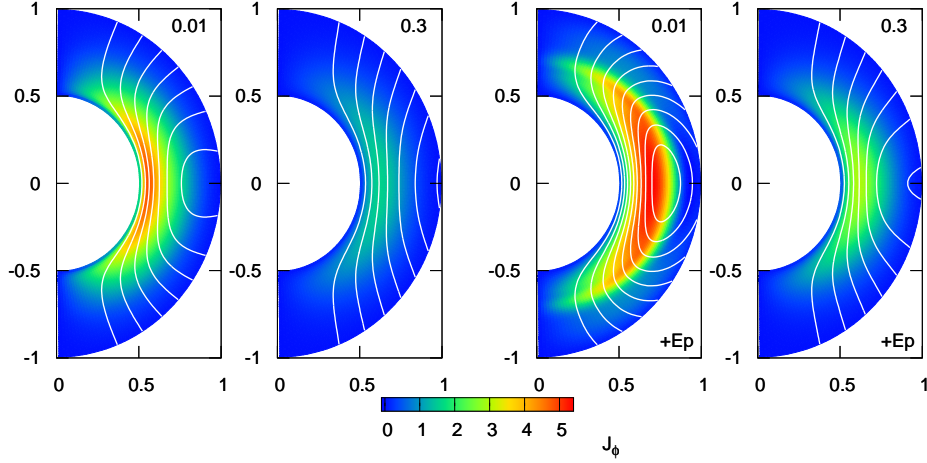


Figure 2. Snapshots of poloidal magnetic function Ψ and azimuthal current j_ϕ at $t = 0.01\tau_H$ and $t = 0.3\tau_H$. Contours of magnetic function represent $\Psi/(B_0 R^2) = 0.07 \times n$ ($n = 1, 2, \dots$). Color indicates strength of azimuthal current $10^{-2} \times 4\pi j_\phi R / (cB_0)$. Left two panels show evolution in barotropic MHD equilibrium. Right two panels present model with extra poloidal magnetic field. It should be noted that crust region ($0.9 \leq r/R \leq 1$) is enlarged five times for display.

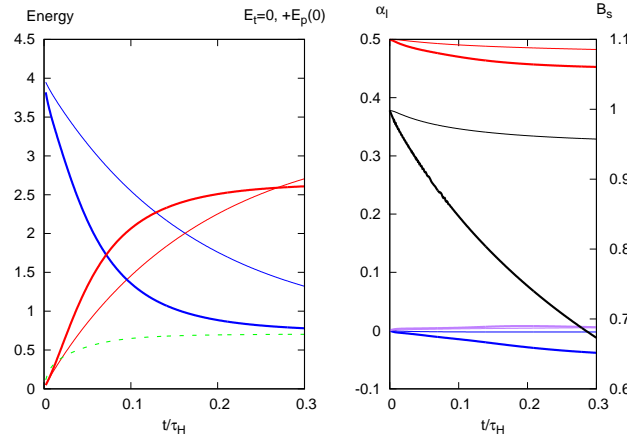


Figure 3. Left panel shows decay of magnetic energy of initial field $\Psi_{(1)} + \Psi_{(2)}$. Magnetic energy $E_B/(B_0^2 R^3)$ is plotted as blue decreasing curve, time-integrated Joule loss as red increasing curve, and work by green dotted curve. Right panel displays variation in magnetic multipole moments, $\alpha_1/(B_0 R^3)$ (in red color), $\alpha_3/(B_0 R^5)$ (in blue color), $\alpha_5/(B_0 R^7)$ (in purple color). Field strength B_r/B_0 at polar surface with right scale is plotted by black curve. Thick curves represent model in which bulk motion is considered.

times, is small. Thus, the evolution of the poloidal energy is almost the same as that in Fig. 1. For the model considering the bulk motion, the increase is insignificant because the energy is also transferred to another channel, i.e., the bulk flow motion. The initial toroidal magnetic energy is converted either to Joule loss or mechanical work. Consequently, the toroidal component rapidly decays; thus, it does not significantly affect the poloidal field evolution.

The right panel of Fig. 4 shows the external multipole moments, $\alpha_l/(B_0 R^{l+2})$, and the field strength, B_s , at the polar caps. Under the initial toroidal magnetic field, multipole components with even number l are produced, so that the relation, $B_r(R, 0) = -B_r(R, \pi)$, is broken, unlike under the dipolar field ($l = 1$). Subsequently, we will discuss the asymmetry of the magnetic field based on Fig. 5. Both $B_r(R, 0)$ and $-B_r(R, \pi)$ are displayed as two curves in Fig. 4. The evolution of the

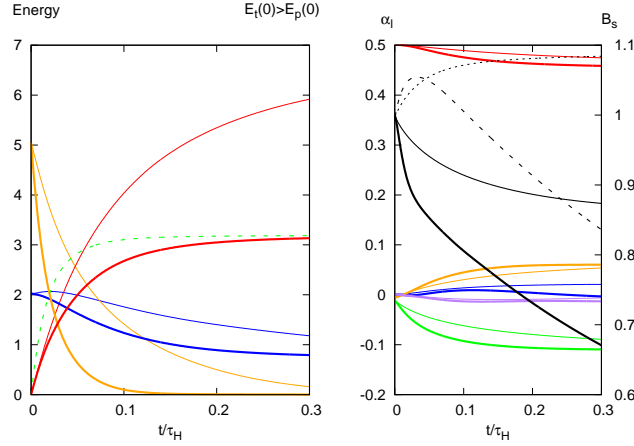


Figure 4. Evolution of magnetic field for initially toroidal-field-dominated model. The left panel shows magnetic energies of poloidal component (in blue color) and toroidal component (in orange color). Time-integrated Joule loss is represented by curve (in red color). Dotted line (in green color) denotes mechanical work for model with bulk flow. Right panel displays time-variation in magnetic multipole moments, $\alpha_1/(B_0 R^3)$ (in red color), $\alpha_2/(B_0 R^4)$ (in green color), $\alpha_3/(B_0 R^5)$ (in blue color), $\alpha_4/(B_0 R^6)$ (in orange color), $\alpha_5/(B_0 R^7)$ (in purple color). Field strength $B_r(R, 0)/B_0$ with right scale is plotted by black line and $-B_r(R, \pi)/B_0$ by black dotted line. Thin line represents result for purely Hall evolution, whereas thick line result with bulk flow.

averaged value, $(|B_r(R, 0)| + |B_r(R, \pi)|)/2$, is similar to the curve in the right panel of Fig. 1. Thus, we find that although the initial toroidal field causes the asymmetry at the surface, it does not change the average strength of the poloidal field.

We demonstrate the magnetic configurations at representative times $t/\tau_H = 0.01$ and 0.1 . Figure 5 shows the poloidal magnetic function, Ψ , as contour lines and the toroidal field, ϖB_ϕ , in color in an enlarged coordinate, $(\xi(r) \sin \theta, \xi(r) \cos \theta)$. The poloidal field in the interior is significantly affected by the strong toroidal component. However, the exterior field is described well by the dipolar one. In the detailed structure, there is asymmetry between the north and south hemispheres in the bottom panels ($t = 0.1\tau_H$). This leads to the difference in the field strengths at the two poles, as shown in the right panels of Fig. 4. The toroidal component rapidly vanishes in the model considering the bulk motion, as shown in the right panels. At time $t/\tau_H = 0.1$, the maximum of B_ϕ decreases to up to 30% of the initial value. The toroidal component does not affect the subsequent evolution once its energy becomes less than that of the poloidal one.

Figure 6 shows behaviors of the Hall velocity $\vec{v}_H \equiv -\vec{j}/(en_e)$ and the bulk velocity \vec{v}_b at $t/\tau_H = 0.01$. The snapshot of the magnetic field corresponds to the right top panel of Fig. 5. Both velocities are normalized by a maximum value $\sim 30R/\tau_H \sim 40 \text{ cm yr}^{-1}$. The tangential components v_θ and v_ϕ are generally larger than radial component: typically $v_r \times R/\Delta r \sim v_\theta \sim v_\phi$. The left top panel of Fig. 6 shows the poloidal component of the Hall velocity. The initial toroidal field $B_\phi > 0$ induces a global circulation of poloidal current, which clockwise flows in $r-\theta$ plane. The direction of the Hall velocity is therefore opposite, and the magnitude becomes small in a deeper region owing to $|v_H| \propto 1/n_e$. The azimuthal component shown in Fig. 6 is also large near the surface, although the current flows in entire crust. In the bottom panels of Fig. 6, the bulk flow velocity is shown. The angular dependence of poloidal velocity-field is approximately dipolar, whereas that of the azimuthal field is quadrupolar. These flow patterns come from the initial toroidal field B_ϕ . The flow velocity \vec{v}_b without it was shown in Fig. 4. of Paper I: quadrupolar in poloidal component $\vec{v}_{b,p}$ and dipolar in azimuthal one $v_{b,\phi}$.

4 EVOLUTION OF QUADRUPOLE DEFORMATION

In this section, we examine the effect of bulk motion on the magnetic deformation, which should evolve with the magnetic field.

4.1 Ellipticity

The irrotational part of the Lorentz force is related to the deviation from a spherical shape. We solve eq.(10) for $\delta\chi$ inside the crust of a neutron star. We assume that the magnetic field does not penetrate the core always. Because the core is spherically symmetric, the boundary condition at the core-crust interface, $r = r_c$, is $\delta\chi = 0$. At the surface, $r = R$, the condition is $\partial\delta\chi/\partial r = 0$, so that $\delta f_r = 0$ in eq. (9). The magnetic deformation in the crust can be estimated using the potential, $\delta\chi$, which may be incorporated as an additional pressure term in eq.(1). The change in an isobaric surface is expressed by the

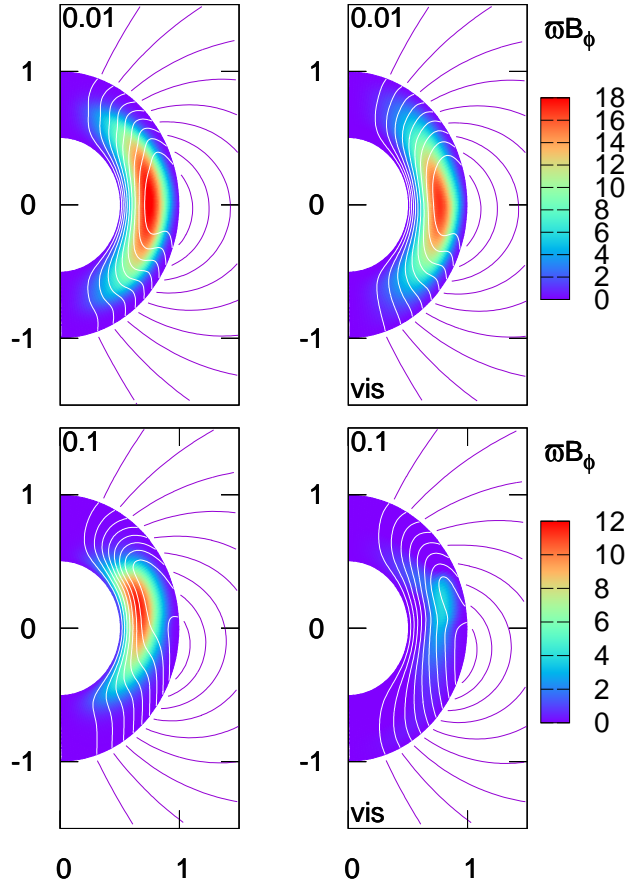


Figure 5. Snapshots of poloidal magnetic function $\Psi/(B_0 R^2)$ by contour lines and current function $\omega B_\phi/(RB_0)$ in color at $t = 0.01\tau_H$ (top) and $t = 0.1\tau_H$ (bottom). Left panels show results of purely Hall evolution, and right panels those of models including bulk motion.

displacement, $\xi(r, \theta)$, which is

$$\xi = -\frac{\delta\chi}{dp/dr} = \frac{\delta\chi r^2}{G\rho M_r}, \quad (15)$$

where a hydrostatic condition (2) is used in the last expression. Using ξ , we estimate the quadrupole deformation of the crustal shape as

$$\epsilon_S = \frac{2\xi(r, \pi/2) - (\xi(r, 0) + \xi(r, \pi))}{2r}. \quad (16)$$

Shape deformation, ϵ_S depends on the radius; therefore, hereafter, we utilize $\bar{\epsilon}_S$, the average value in the crust.

$$\bar{\epsilon}_S = 10^{-6} \epsilon_* \left(\frac{B_0}{5 \times 10^{13} \text{G}} \right)^2, \quad (17)$$

where we use the canonical values for the mass ($M = 1.4M_\odot$) and radius ($R = 12\text{km}$) of a neutron star. The coefficients, ϵ_* , are numerically calculated for the evolving models.

The quadrupole deformation is important in spin-down evolution of a pulsar, and hence, also for gravitational wave astronomy (e.g. Gao et al. 2017; Kalita & Mukhopadhyay 2019). The ellipticity, ϵ_Q , is defined by the quadrupole moment as follows:

$$\epsilon_Q \equiv \frac{I_{xx} - I_{zz}}{\bar{I}}, \quad (18)$$

where $I_{ij} = \int \rho x_i x_j d^3x$ and \bar{I} is the average of I_{ij} . The ellipticity, ϵ_Q depends on the entire stellar structure. Our consideration of the deformation is limited to the crustal part of a star, which leads to the difference in the numerator of eq.(18). The typical mass (or mass density) relevant to the numerator is the crustal mass, ΔM , whereas that for the denominator is the stellar mass, M . The ellipticity, ϵ_Q , is estimated as

$$\epsilon_Q \approx \frac{\Delta M}{M} \bar{\epsilon}_S \approx 10^{-2} \times \bar{\epsilon}_S, \quad (19)$$

where ΔM is $\sim 10^{-2}M$ for a typical model. Note that an exact value of ϵ_Q is not obtained without a specified stellar model.

We discuss the evolution of the magnetic deformation of a neutron star. Figure 7 shows the normalized ellipticity, ϵ_* ($\propto \bar{\epsilon}_S$),

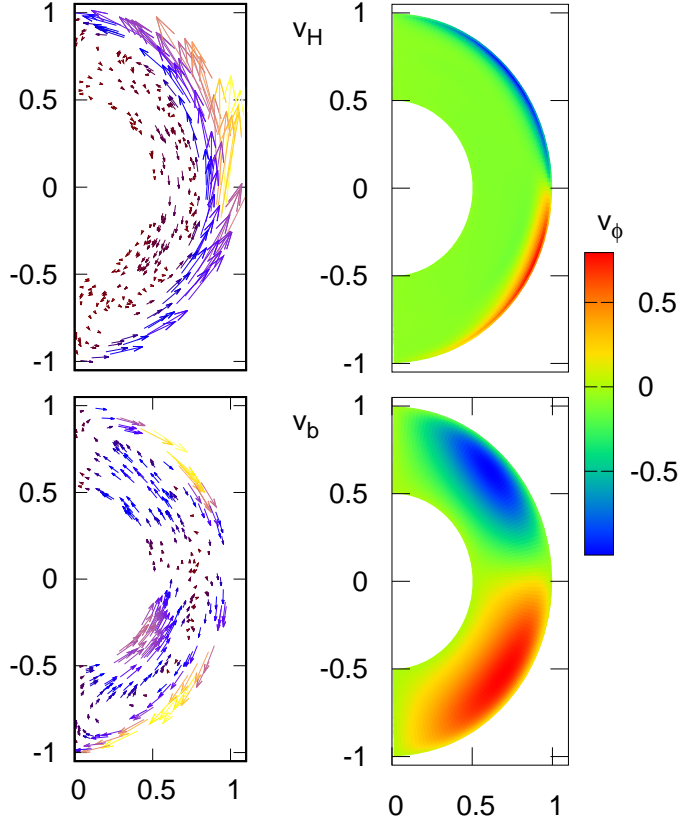


Figure 6. Snapshot of velocity fields \vec{v}_H (top) and \vec{v}_b (bottom). Left panels show poloidal components at randomly selected grid points, and right panels show normalized azimuthal-component by color contour.

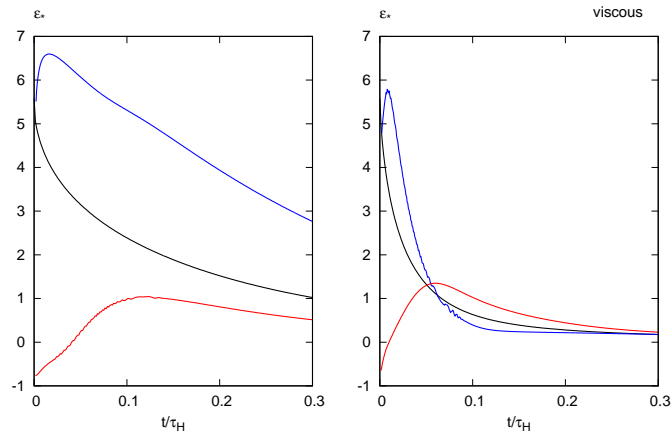


Figure 7. Evolution of magnetic deformation. Central curve in black color represents fiducial model described in Section 3.1. Model initially containing a loop, as discussed in Section 3.2, is represented by blue curve, and toroidal-field-dominated model described in Section 3.3 is denoted by a red curve. In latter case, ϵ_* is initially negative. Left panel shows results for Hall evolution, and right one for those with bulk motion.

numerically calculated for our crustal model. It is well known that a poloidal magnetic field produces an oblate shape ($\bar{\epsilon}_S > 0$), whereas a toroidal field a prolate one ($\bar{\epsilon}_S < 0$). For the fiducial model, as described in Section 3.1, ϵ_* is always positive and monotonically decreases with time. The value at $t/\tau_H = 0.3$ decreases to $\sim 20\%$ of that with the initial model. This decrease in ϵ_* originates from the decrease in the magnetic energy or magnetic pressure. For the model containing a loop, as discussed in Section 3.2, the Lorentz force from the extra part initially added by $\Psi_{(2)}$ is canceled when calculating the quadrupole deformation throughout the crust. According to the prompt redistribution of the current, the deformation increases at $t/\tau_H \sim 0.01$. With further loss of the magnetic energy, the deformation gradually decreases. The initial value of ϵ_* is negative for the toroidal-field-dominated model described in Section 3.3. The associated prolate shape changes to an oblate one based on the magnetic field evolution. The change in the sign of ϵ_* broadly corresponds to the turning point of the dominant component. The decay timescales of the poloidal and toroidal fields are different. The toroidal field decays more rapidly than the poloidal one, which causes the change from the prolate to an oblate shape on a secular timescale.

In the right panel of Fig. 7, we show the evolution of the magnetic deformation for the models considering a viscous bulk motion. As presented in Figs. 1, 3, and 4, the magnetic energy is converted into the fluid kinetic energy and the Joule heat, which are of the same order. The decay timescale becomes approximately half. This rapid dissipation of the magnetic energy shortens the evolutionary timescale of ϵ_* , as shown in Fig. 7.

4.2 Discussion

Suvorov et al. (2016) already considered the evolution of the quadrupole ellipticity caused by the Hall drift in a neutron star crust. Our methods and models significantly differ from those used by them; therefore, a comparison of the numerical results is difficult. Their evolution model is based on a relatively detailed magneto-thermal calculation. The most crucial difference is with their mathematical method for evaluating the ellipticity. They calculated the quadrupole deviation based on a nonbarotropic nature. Specifically, the quadrupole moment, $\delta I_{ij} = \int \delta \rho x_i x_j d^3x$, was calculated for a nonspherical perturbation $\delta \rho$ of the density induced by a 'curl' of the Lorentz force (Mastrano et al. 2013, 2015). This corresponds to the solenoidal part of the Lorentz force and induces a circulation of the viscous fluid, as discussed in Section 2. In our treatment, the quadrupole deviation is calculated from the irrotational part of the force. When we apply their method to our initial model in the barotropic MHD equilibrium, the ellipticity is exactly zero. However, our method yields $\epsilon_Q \approx 10^{-8} (B_0/5 \times 10^{13} \text{G})^2$ in eq.(19). Therefore, two methods generate significantly different ellipticities. Moreover, the time evolution of the deformation in their models is complex. No clear relationships between the ellipticity and the maximum amplitude of the poloidal or toroidal magnetic field are revealed in their results. In the present treatment, the quadrupole deformation, ϵ_Q , gradually decreases with the magnetic energy, E_B , although ϵ_Q is not exactly proportional to E_B . The oblate or prolate shape of the deformation depends on whether the dominant magnetic field is poloidal or toroidal.

The ellipticity, ϵ_Q in eq.(19) coincides with the energy ratio, E_B/E_G , where the magnetic energy stored in the crust is $E_B \approx 6 \times 10^{45} (B_0/5 \times 10^{13} \text{G})^2 \text{erg}$ and the gravitational binding energy of the star is $E_G \approx 3 \times 10^{53} \text{erg}$. This relation between the quadrupole deformation and the energy ratio has been confirmed by various models, irrespective of the equation of states and the relativistic factor, and presented in the literature (e.g., Ferraro 1954; Bonazzola & Gourgoulhon 1996; Konno et al. 1999; Ioka 2001; Yoshida & Eriguchi 2006; Haskell et al. 2008; Lander & Jones 2009; Uryū et al. 2014, 2019). In the previous models, the magnetic field extends into the whole interior³. However, it is localized to the outer part in our model. We found that the empirical relation between quadrupole deformation and energy ratio is still applicable.

5 CONCLUDING REMARKS

In this study, we consider the effects of bulk motion on the magnetic field evolution in a neutron star crust. Particularly, the decay of both the surface dipole and the magnetic deformations are explored. Their evolution is always accelerated by the energy loss to the bulk flow as a new channel.

Consequently, the deformation in the crust shrinks with decreasing magnetic energy. The toroidal and higher poloidal components decay on a smaller timescale than that of the dipolar component. Finally, the quadrupole deformation is determined by the long-lived dipole. From our numerical simulation, we also find that the deformation is a good indicator of magnetic energy stored in the interior. The shape is prolate when the toroidal component is initially dominated, whereas it becomes oblate when the poloidal component is dominated. The ratio of the magnetic energy to the gravitational binding energy provides the ellipticity. Specifically, the magnetic energy of the dipole component ($l = 1$) is important because the quadrupole deformation, which corresponds to the spherical harmonics index, $l = 2$, is related to the magnetic field at $l = 1$. The contribution from higher order components with $l > 1$ is partially canceled by the spatial integration.

³ The ellipticity depends on the field strength as $\epsilon_Q \propto B^2$, but it changes as $\epsilon_Q \propto BH_c$ for a neutron star containing a type II superconducting core, where H_c is the critical field (Lander 2013)

The magnetic field evolution depends on the initial configurations, which are less clear. The dynamical stability of a magnetized star is a long-standing unsolved problem (e.g., Braithwaite & Nordlund 2006; Lander & Jones 2012; Ciolfi & Rezzolla 2013; Sur et al. 2020). Some MHD calculations suggest stable models of twisted torus, a configuration comprised of poloidal and toroidal components. They are based on a whole star without a crust, and the formation and stability of the localized fields is unclear. As plausible states at the birth of a magnetized star, we consider a barotropic MHD equilibrium model and its variants. The crustal magnetic field, which initially satisfies the MHD equilibrium, evolves toward the Hall equilibrium. The difference between the two equilibria originates from the different distributions of the mass and electron number densities (Gourgouliatos et al. 2013; Fujisawa & Kisaka 2014). The spatial profile is not significantly different; therefore, the transition from the barotropic MHD to the Hall equilibria is not extremely drastic. To examine the effect of the initial field configuration, we add poloidal and toroidal fields as extra components and compare the evolution. Our initial model presented in this paper is an ad hoc method to demonstrate the difference on a secular timescale. Owing to the extra poloidal or toroidal components, different evolutionary features are expected; however, our results show that the extra components vanish and do not have a significant effect. We find that the surface dipole field given by the barotropic MHD equilibrium is almost stable, not changing significantly in $\sim 10^6$ years. A counter example can be easily considered. Let us suppose that the electric current relevant to the dipole field is localized near the surface where the electric conductivity is low. For this case, the bulk motion is also effective in that region owing to the low viscosity there (Lander & Gourgouliatos 2019; Kojima & Suzuki 2020). The decay timescale correspondingly becomes shorter, even less than 10^5 yr for the extreme configurations.

In summary, evolutionary models for a simple magnetic field are obtained under the assumption that the initial model comprises ordered smooth fields in near-MHD equilibrium. By relaxing the above assumption, we expect that a rapid change in the locally irregular components will lead to diverse evolutionary behaviors.

ACKNOWLEDGEMENTS

This work was supported by JSPS KAKENHI Grant Number JP17H06361, JP19K03850(YK), JP18H01245, JP18H01246, JP19K14712 (SK), JP20H04728 (KF).

DATA AVAILABILITY

The data underlying this article will be shared on reasonable request to the corresponding author.

REFERENCES

- Baiko D. A., Chugunov A. I., 2018, *MNRAS*, **480**, 5511
 Bonazzola S., Gourgoulhon E., 1996, *A&A*, **312**, 675
 Braithwaite J., Nordlund Å., 2006, *A&A*, **450**, 1077
 Bransgrove A., Levin Y., Beloborodov A., 2018, *MNRAS*, **473**, 2771
 Castillo F., Reisenegger A., Valdivia J. A., 2017, *MNRAS*, **471**, 507
 Castillo F., Reisenegger A., Valdivia J. A., 2020, *MNRAS*,
 Chugunov A. I., Horowitz C. J., 2010, *MNRAS*, **407**, L54
 Ciolfi R., Rezzolla L., 2013, *MNRAS*, **435**, L43
 Elfritz J. G., Pons J. A., Rea N., Glampedakis K., Viganò D., 2016, *MNRAS*, **456**, 4461
 Enoto T., Kisaka S., Shibata S., 2019, *Reports on Progress in Physics*, **82**, 106901
 Ferraro V. C. A., 1954, *ApJ*, **119**, 407
 Fujisawa K., Kisaka S., 2014, *MNRAS*, **445**, 2777
 Gao H., Cao Z., Zhang B., 2017, *ApJ*, **844**, 112
 Glampedakis K., Jones D. I., Samuelsson L., 2011, *MNRAS*, **413**, 2021
 Goldreich P., Reisenegger A., 1992, *ApJ*, **395**, 250
 Gourgouliatos K. N., Cumming A., 2014a, *Phys. Rev. Lett.*, **112**, 171101
 Gourgouliatos K. N., Cumming A., 2014b, *MNRAS*, **438**, 1618
 Gourgouliatos K. N., Hollerbach R., 2018, *ApJ*, **852**, 21
 Gourgouliatos K. N., Cumming A., Reisenegger A., Armaza C., Lyutikov M., Valdivia J. A., 2013, *MNRAS*, **434**, 2480
 Gourgouliatos K. N., Wood T. S., Hollerbach R., 2016, *Proceedings of the National Academy of Science*, **113**, 3944
 Graber V., Andersson N., Glampedakis K., Lander S. K., 2015, *MNRAS*, **453**, 671
 Gugercinolu E., Alpar M. A., 2016, *MNRAS*, **462**, 1453
 Gusakov M. E., 2019, *MNRAS*, **485**, 4936
 Gusakov M. E., Kantor E. M., Ofengeim D. D., 2017, *Phys. Rev. D*, **96**, 103012
 Haskell B., Samuelsson L., Glampedakis K., Andersson N., 2008, *MNRAS*, **385**, 531
 Horowitz C. J., Kadau K., 2009, *Phys. Rev. Lett.*, **102**, 191102
 Ioka K., 2001, *MNRAS*, **327**, 639
 Ioka K., 2020, arXiv e-prints, p. [arXiv:2008.01114](https://arxiv.org/abs/2008.01114)

- Kalita S., Mukhopadhyay B., 2019, *MNRAS*, **490**, 2692
- Kantor E. M., Gusakov M. E., 2017, *MNRAS*, **473**, 4272
- Kojima Y., Kisaka S., 2012, *MNRAS*, **421**, 2722
- Kojima Y., Suzuki K., 2020, *MNRAS*, **494**, 3790
- Konno K., Obata T., Kojima Y., 1999, *A&A*, **352**, 211
- Lander S. K., 2013, *Phys. Rev. Lett.*, **110**, 071101
- Lander S. K., 2016, *ApJ*, **824**, L21
- Lander S. K., Gourgouliatos K. N., 2019, *MNRAS*, **486**, 4130
- Lander S. K., Jones D. I., 2009, *MNRAS*, **395**, 2162
- Lander S. K., Jones D. I., 2012, *MNRAS*, **424**, 482
- Lander S. K., Andersson N., Antonopoulou D., Watts A. L., 2015, *MNRAS*, **449**, 2047
- Li X., Levin Y., Beloborodov A. M., 2016, *ApJ*, **833**, 189
- Marchant P., Reisenegger A., Valdivia J. A. r., Hoyos J. H., 2014, *ApJ*, **796**, 94
- Mastrano A., Lasky P. D., Melatos A., 2013, *MNRAS*, **434**, 1658
- Mastrano A., Suvorov A. G., Melatos A., 2015, *MNRAS*, **447**, 3475
- Ofengeim D. D., Gusakov M. E., 2018, *Phys. Rev. D*, **98**, 043007
- Passamonti A., Akgün T., Pons J. A., Miralles J. A., 2017, *MNRAS*, **469**, 4979
- Pons J. A., Geppert U., 2007, *A&A*, **470**, 303
- Sur A., Haskell B., Kuhn E., 2020, *MNRAS*, **495**, 1360
- Suvorov A. G., Kokkotas K. D., 2019, *MNRAS*, **488**, 5887
- Suvorov A. G., Kokkotas K. D., 2020, *Phys. Rev. D*, **101**, 083002
- Suvorov A. G., Mastrano A., Geppert U., 2016, *MNRAS*, **459**, 3407
- Tomimura Y., Eriguchi Y., 2005, *MNRAS*, **359**, 1117
- Turolla R., Zane S., Watts A. L., 2015, *Reports on Progress in Physics*, **78**, 116901
- Uryū K., Gourgoulhon E., Markakis C. M., Fujisawa K., Tsokaros A., Eriguchi Y., 2014, *Phys. Rev. D*, **90**, 101501
- Uryū K., Yoshida S., Gourgoulhon E., Markakis C., Fujisawa K., Tsokaros A., Taniguchi K., Eriguchi Y., 2019, *Phys. Rev. D*, **100**, 123019
- Viganò D., Rea N., Pons J. A., Perna R., Aguilera D. N., Miralles J. A., 2013, *MNRAS*, **434**, 123
- Viganò D., et al., 2019, *Computer Physics Communications*, **237**, 168
- Wood T. S., Hollerbach R., 2015, *Phys. Rev. Lett.*, **114**, 191101
- Yoshida S., Eriguchi Y., 2006, *ApJS*, **164**, 156